Figures and figure supplements

Pivotal role for skin transendothelial radio-resistant anti-inflammatory macrophages in tissue repair

Olga Barreiro *et al*

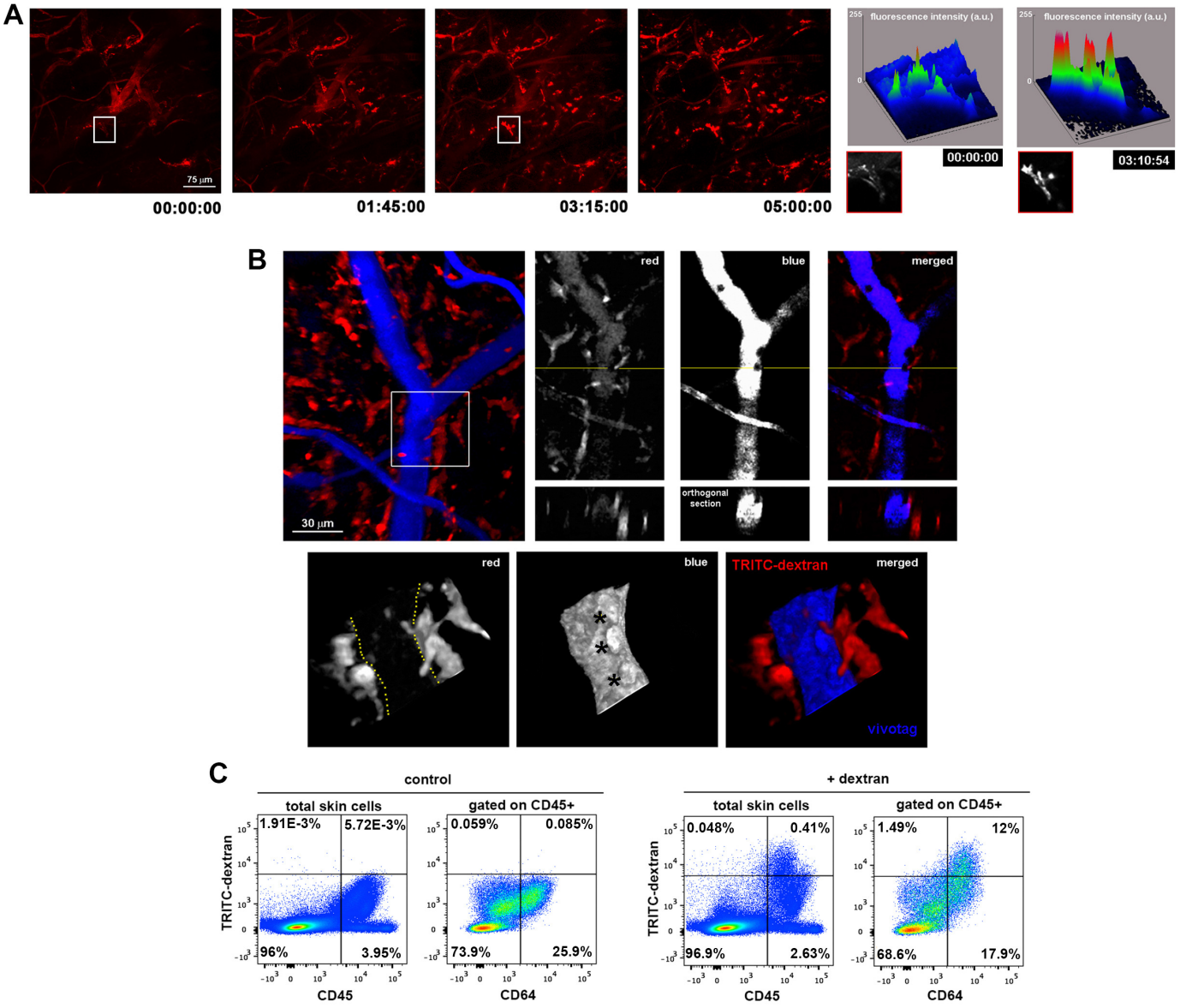

Figure 1. Dermal perivascular macrophages capture intraluminal dextran. (**A**) (Left) Representative frames from ***Video 1*** are shown. Briefly, image acquisition of ear mouse dermis started 30 min after i.v. injection of HMw TRITC-dextran and lasted for 5 hr. (Right) The surface plots show the fluorescence intensity of a representative cell at the starting time and 3 hr 15 min later (white insets in corresponding video frames; a.u., arbitrary units). (**B**) (Upper left) Three-dimensional (3D) rendering of the fluorescence signals obtained in a C57BL/6 ear dermis after i.v. administration of HMw TRITC-dextran (red, injected 16 hr before imaging) and vivotag (blue, injected at the time of imaging). (Upper right) The panels show a representative xy plane split into the different channels with an orthogonal section beneath, obtained along the yellow cross-section line. (Lower) The boxed region in the 3D rendering is shown tilted and at higher magnification. Yellow-dotted line marks endothelial perimeter in the red channel. Black asterisks mark void spaces corresponding to intravascular cells in the blue channel. (**C**) Phenotypic analysis of the dextran^{+} cells in the ear skin using the pan-leukocyte marker CD45 and the macrophage marker CD64. Representative FACS dot plots of control and HMw TRITC-dextran-injected mice are shown (n = 4).
DOI: 10.7554/eLife.15251.003

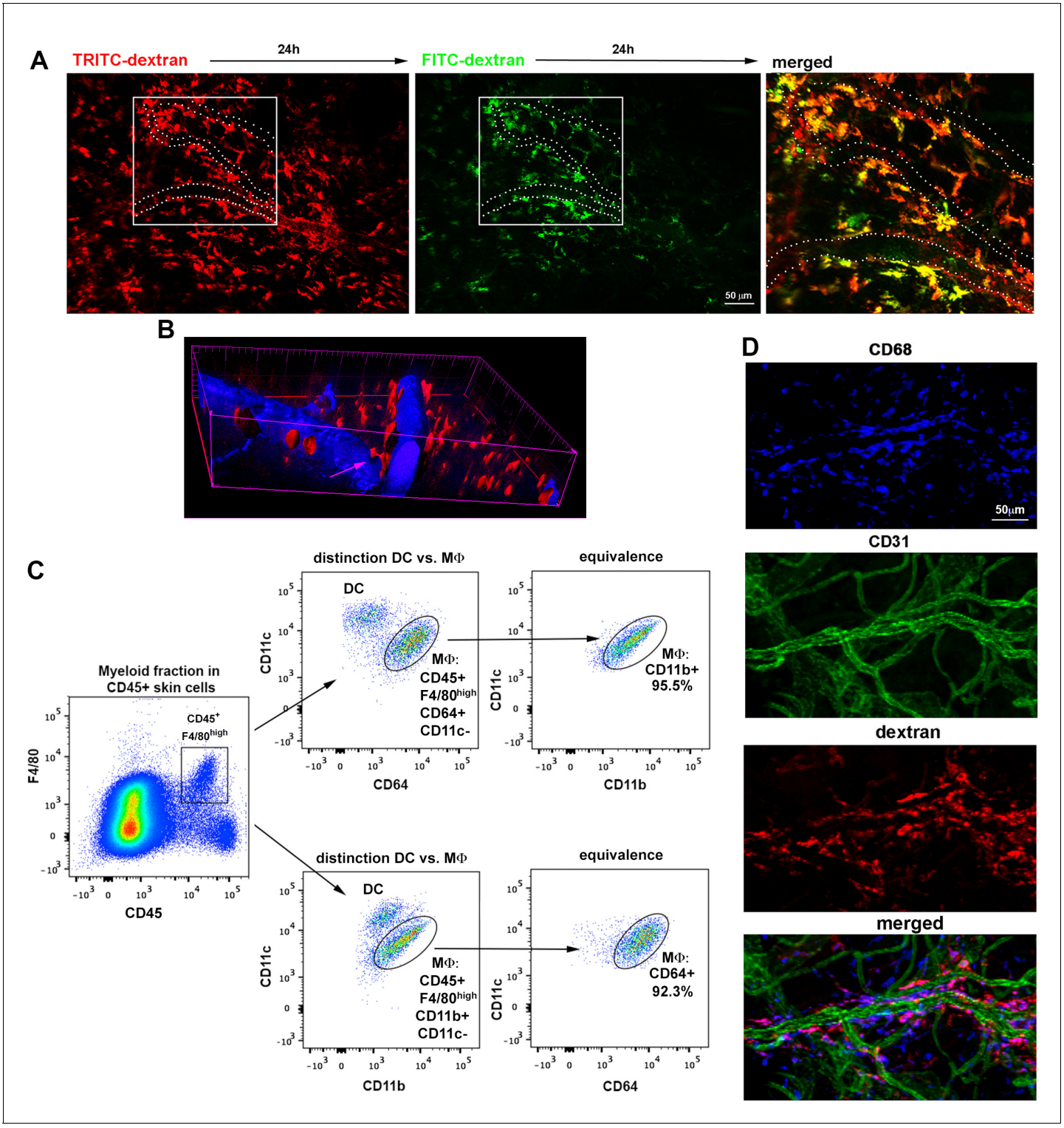

Figure 1—figure supplement 1. Spatio-temporal analysis of endothelial-protruding macrophages under steady-state conditions. (**A**) 'Dextran pulse-chase' assay. A C57BL/6 mouse was sequentially injected with red and green HMw dextran (24 hr interval) and then sacrificed 48 hr after the beginning of the experiment. A maximal projection of the mouse ear dermis split in green and red channels as well as a zoomed merged image of the inset are shown. Some of the vessels in the inset have been depicted with white dotted lines for reference. (**B**) Orthogonal sectioning of the isosurface rendering from data shown in ***Figure 1B***. The pink arrow highlights the interaction of a dextran^{+} cell (red) with an intravascular cell (black hole not filled with the blue vascular tracer). (**C**) Representative FACS analysis describing the specific identification of skin macrophages by means of two equivalent staining strategies that only differ in the use of either CD11b or CD64 (MΦ: macrophages, DC: dendritic cells). (**D**) Whole-mount staining of the ear of a C57BL/6

Figure 1—figure supplement 1 continued on next page

Figure 1—figure supplement 1 continued

mouse injected i.v. with HMw TRITC-dextran (red), using anti-CD68 (macrophage marker, blue) and anti-CD31 (vascular marker, green). Split channels and the merged composite of the maximal projection image obtained from a z-stack of the dermis are shown.

DOI: 10.7554/eLife.15251.004

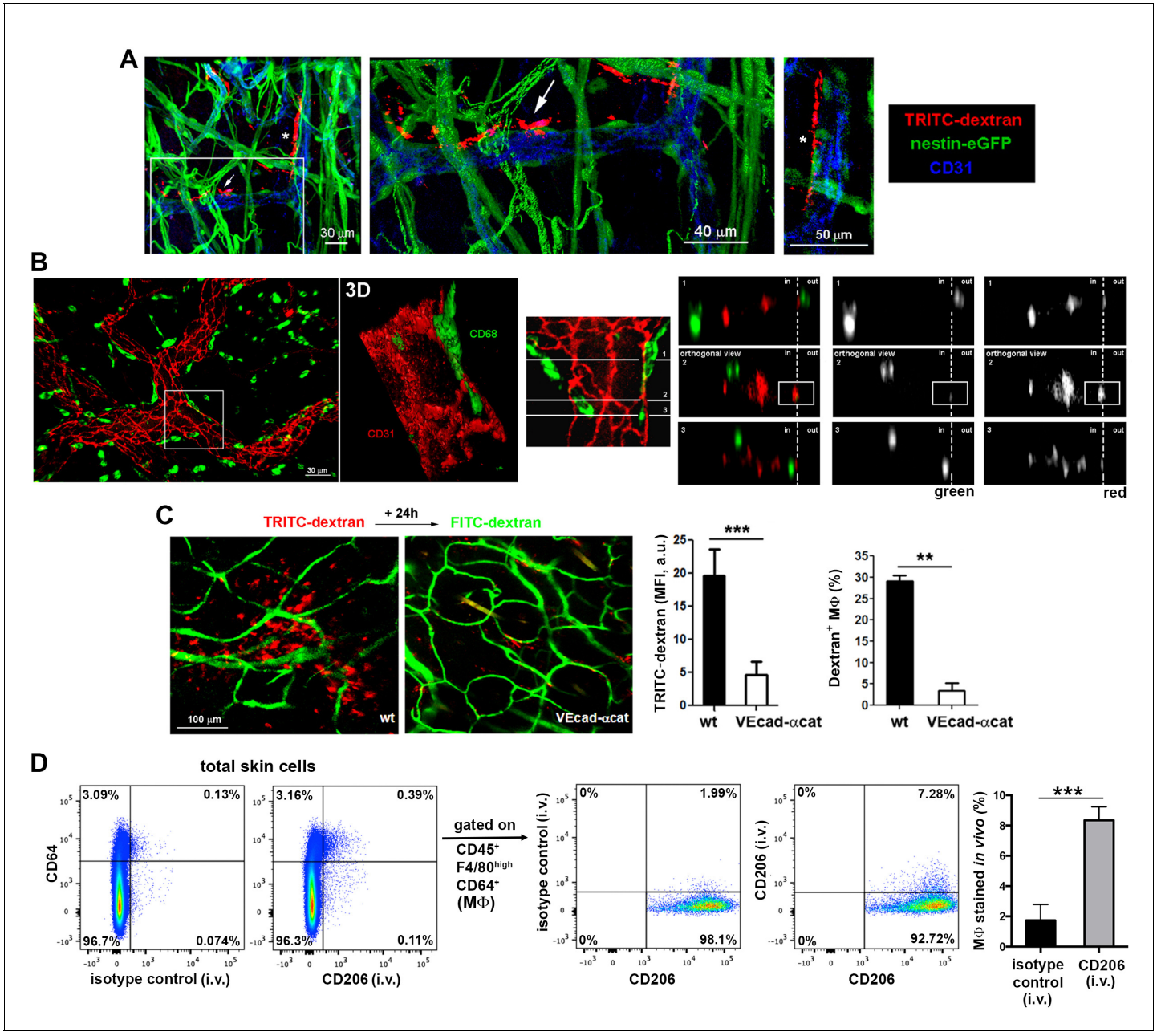

Figure 2. Dermal perivascular macrophages protrude across endothelial junctions into microvessels. (**A**) (Left) 3D reconstruction combining fluorescence signal and isosurface rendering of the ear dermis of a nestin-eGFP animal injected i.v. with HMw dextran. The inset is shown magnified in the central panel with a dextran^{+} macrophage protruding into the vascular lumen highlighted with a white arrow. Another protruding macrophage, marked with an asterisk in the 3D reconstruction image, is shown in a zoomed single confocal plane on the right. (**B**) (Left) Whole-mount staining of a C57BL/6 ear using anti-CD31 (red) and anti-CD68 (green) antibodies. (Center) The inset is shown as a 3D rendering with higher magnification. (Right) The same inset was tilted and further analyzed by orthogonal sectioning. The white cross-section lines are localized along the cell body and the intravascular protrusion of the macrophage on the right side. (in, intraluminal; out, extravascular). (**C**) Comparison of dextran capture in wt vs. VE-cadherin-α-cat mice under steady-state conditions. Animals were injected i.v. with HMw TRITC-dextran and with HMw FITC-dextran 24 hr later, before imaging. (Left) Representative intravital images show the dermis of each phenotype, containing dextran^{+} cells (red) and vasculature (green). (Center) The bar histogram represents the mean fluorescence intensity (MFI) of the TRITC-dextran signal ± SD obtained from five 20x fields of view of 2 animals of each phenotype (a.u., arbitrary units). (Right) Flow cytometry analysis of dextran capture by macrophages in wt and VE-cad-α-cat mice. Statistical significance was assessed by unpaired two-tailed Student's t-test (**p-value < 0.005, ***p-value < 0.001). (**D**) In vivo staining of the intraluminal protrusions of endothelium-protruding macrophages. Mice were injected i.v. with either an antibody against CD206 (mannose receptor, involved in dextran uptake) or an isotype control antibody and sacrificed 3 min later. Then, animals were perfused with PBS and ears were processed for FACS analysis. Single-cell suspensions were stained with anti-CD45, anti-F4/80, anti-CD64 and a different anti-CD206 clone. Representative FACS dot plots

Figure 2 continued on next page

Figure 2 continued

are depicted and the bar histogram shows the specific detection of macrophage staining in vivo (MΦ: macrophages). Data are mean values ± SD (n = 4). Statistical significance was assessed by unpaired two-tailed Student's t-test (***p<0.001).

DOI: 10.7554/eLife.15251.010

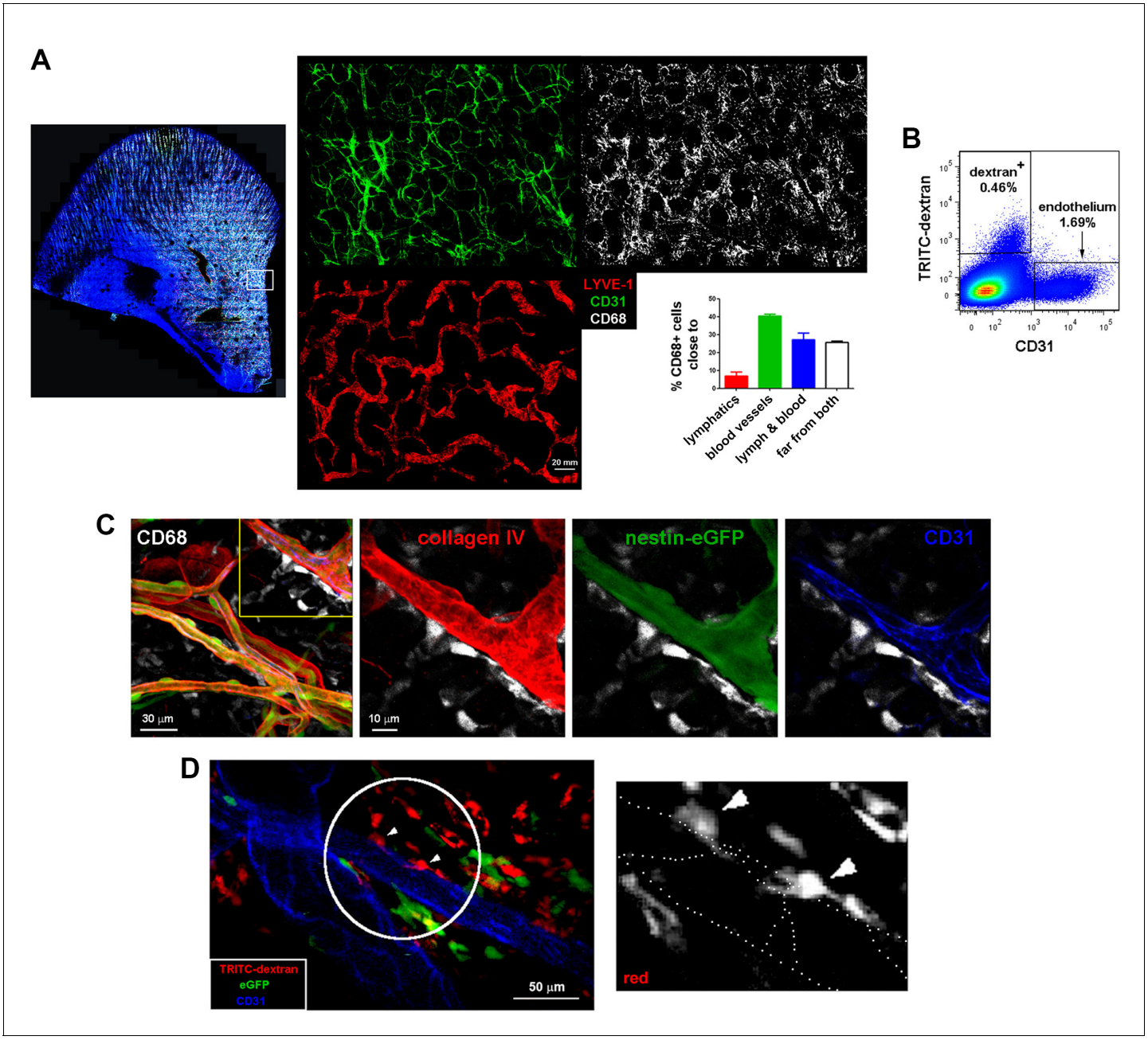

Figure 2—figure supplement 1. Spatial organization of skin macrophages relative to lymphatic and blood vessels. (**A**) Mesoscopic analysis of the spatial distribution of skin-resident macrophages relative to microvasculature and lymphatics. (Left) Whole-mount staining of a C57BL/6 mouse ear using anti-CD68 (white), anti-CD31 (green), anti-LYVE-1 (red) and DAPI. The maximal projection of the tiled z-stacks is shown. (Right) Split channels from the region in the inset are shown with higher magnification. The bar histogram represents the percentage of macrophages ($CD68^+$ cells) proximal to either lymphatics or blood vessels obtained by 3D computational analysis of distances. (**B**) A single-cell suspension of ears from a C57BL/6 animal injected i.v. with HMw TRITC-dextran was stained with an specific marker for endothelium (CD31) and analyzed by FACS. (**C**) Maximal projection of a z-stack of skin dermis from a nestin-eGFP mouse ear showing macrophages ($CD68^+$, white) on the outer surface of vessel walls, which are defined by basal lamina staining (collagen IV, red), pericytes ($eGFP^+$ cells covered with collagen) and endothelium (CD31, blue). The boxed area is shown as a magnified view with split channels. (**D**) Intravital imaging of the dermis of a chimeric animal (B6 ACTB-eGFP (donor)/C57BL/6 (host)) that was injected i.v. with HMw TRITC-dextran and anti-CD31 Alexa647 (extracted from ***Video 6***). (Left) A single confocal plane is shown. The white circle and arrowheads highlight $dextran^+$ macrophages whose protrusions are aligned with endothelial junctions. (Right) The red signal of these cells is displayed with zoom. Endothelial junctions are depicted with white dotted lines.

DOI: 10.7554/eLife.15251.011

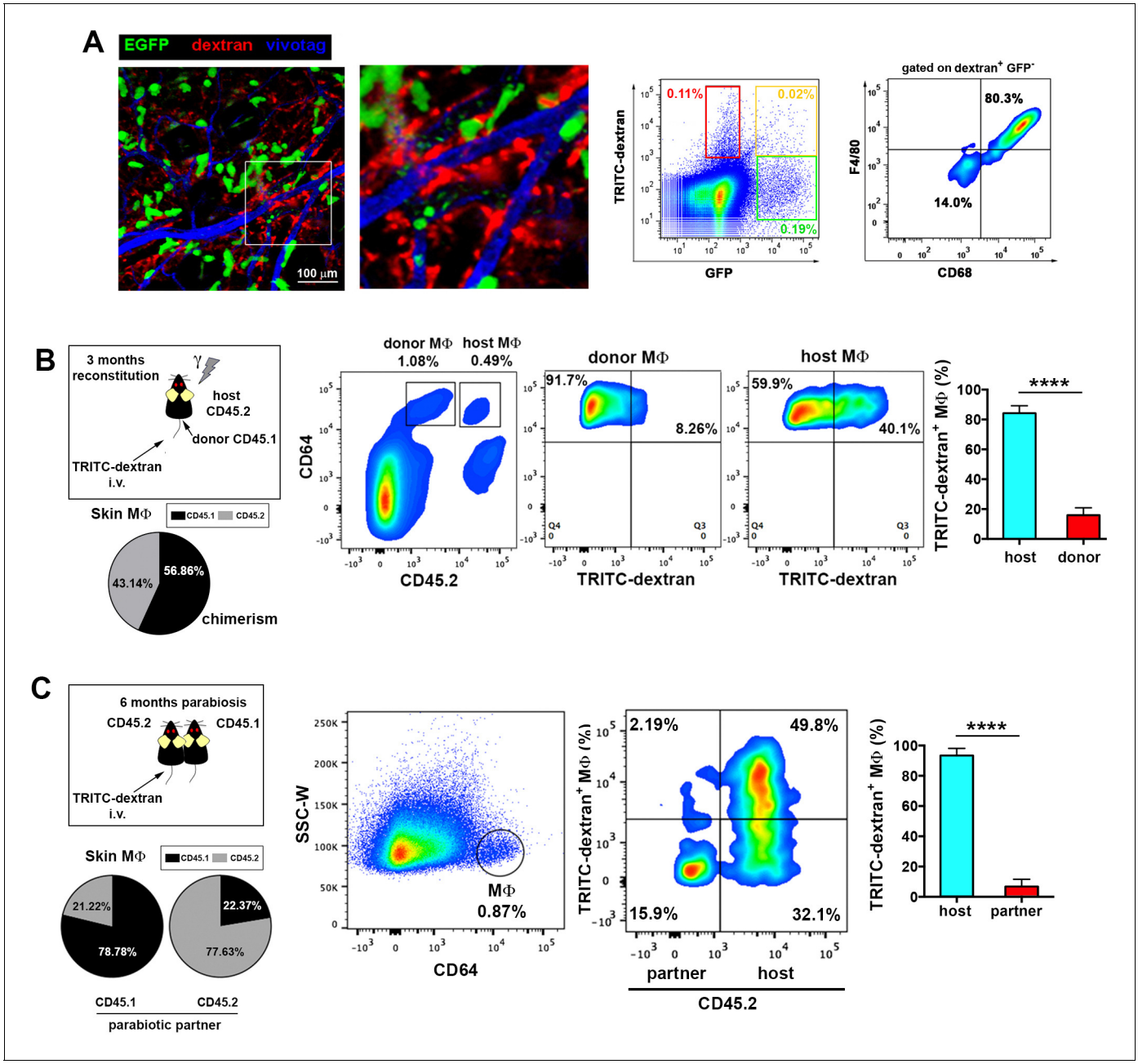

Figure 3. Endothelium-protruding macrophages are radio-resistant macrophages independent of BM supply. (**A**) (Left) Representative intravital image (maximal projection of a z-stack), with zoomed view aside, of the ear dermis of a chimeric B6 ACTB-eGFP (donor, green)/C57BL/6 (host) animal pre-treated with HMw TRITC-dextran (red) and injected with vivotag (blue) at the time of imaging. The 3D colocalization analysis between green and red signals was estimated (Pearson's coefficient in colocalized volume = 0.1074). (Right) Representative FACS dot plots showing the analysis of the TRITC-dextran$^+$ (red), the GFP$^+$ (green) and the double positive subsets in these chimeric animals as well as the macrophage content in the TRITC-dextran$^+$ subset. (**B**) (Left) Averaged frequency of CD45.1$^+$ (donor) and CD45.2$^+$ (host) skin-resident macrophages in chimeric animals reconstituted for 3 months. (Right) Representative FACS analysis of the dextran$^+$ subset in chimeric CD45.1 (donor)/CD45.2 (host) animals treated with HMw TRITC-dextran. The bar histogram shows the contribution of host and donor macrophages to the pool of dextran$^+$ macrophages in the skin. Values are mean ± SD (n=4). Statistical significance was assessed by unpaired two-tailed Student's t-test (****p<0.0001). (**C**) Parabionts were injected i.v. with HMw TRITC-dextran and sacrificed 3d later. Ears were harvested and processed for FACS analysis. (Left) Averaged frequency of CD45.1$^+$ and CD45.2$^+$ skin-resident macrophages in each partner of the parabiotic pairs (n = 4) after 6 months of parabiosis. (Right) Representative dot plots and bar histogram showing the contribution of host macrophages and macrophages derived from partner to the pool of dextran$^+$ macrophages in the skin. Values are mean ± SD (n = 4). Statistical significance was assessed by unpaired two-tailed Student's t-test (****p<0.0001).

DOI: 10.7554/eLife.15251.013

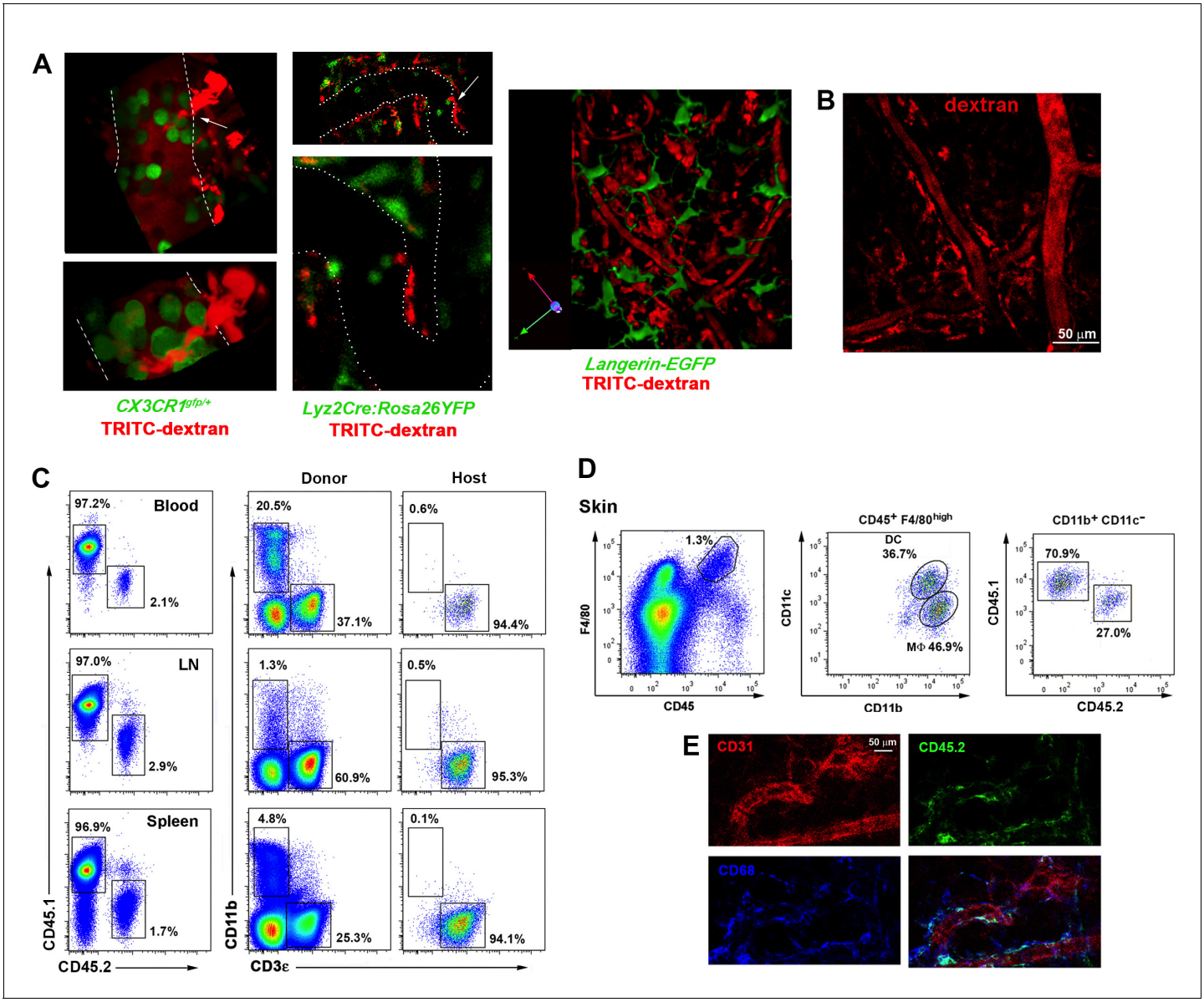

Figure 3—figure supplement 1. Analysis of tissue-resident macrophage subsets in reporter and chimeric animals. (**A**) Dextran^{+} macrophages do not express GFP in several myeloid reporter mouse lines. *Cx3cr1*$^{gfp/+}$, *Lyz2*-Cre:Rosa26YFP (also known as *LysM*-Cre:Rosa26YFP) and Langerin-eGFP animals were injected HMw TRITC-dextran i.v. and intravital imaging of ear dermis in steady-state was performed. Panels either show representative confocal planes, maximal projections or 3D reconstructions. White dashed lines or white dots depict vessel walls and white arrows highlight contacts of protruding macrophages and intravascular GFP^{+} cells. (**B**) Intravital imaging of ear dermis from a mouse injected with HMw TRITC-dextran i.v. 7d after lethal γ-irradiation. (**C**) Representative FACS analysis of the frequency of CD45.1^{+} (donor) and CD45.2^{+} (host) myeloid and T-lymphoid subsets in different organs (blood, lymph nodes and spleen) of a chimeric animal after 3 months of reconstitution. (**D**) Representative FACS analysis of skin donor and host myeloid subsets in the same chimeric animal. (**E**) Images represent the maximal projection of a z-stack acquired in a fixed ear dermis of a chimeric mouse, showing CD45.2 (green), CD68 (blue) and CD31 (red) stainings.

DOI: 10.7554/eLife.15251.014

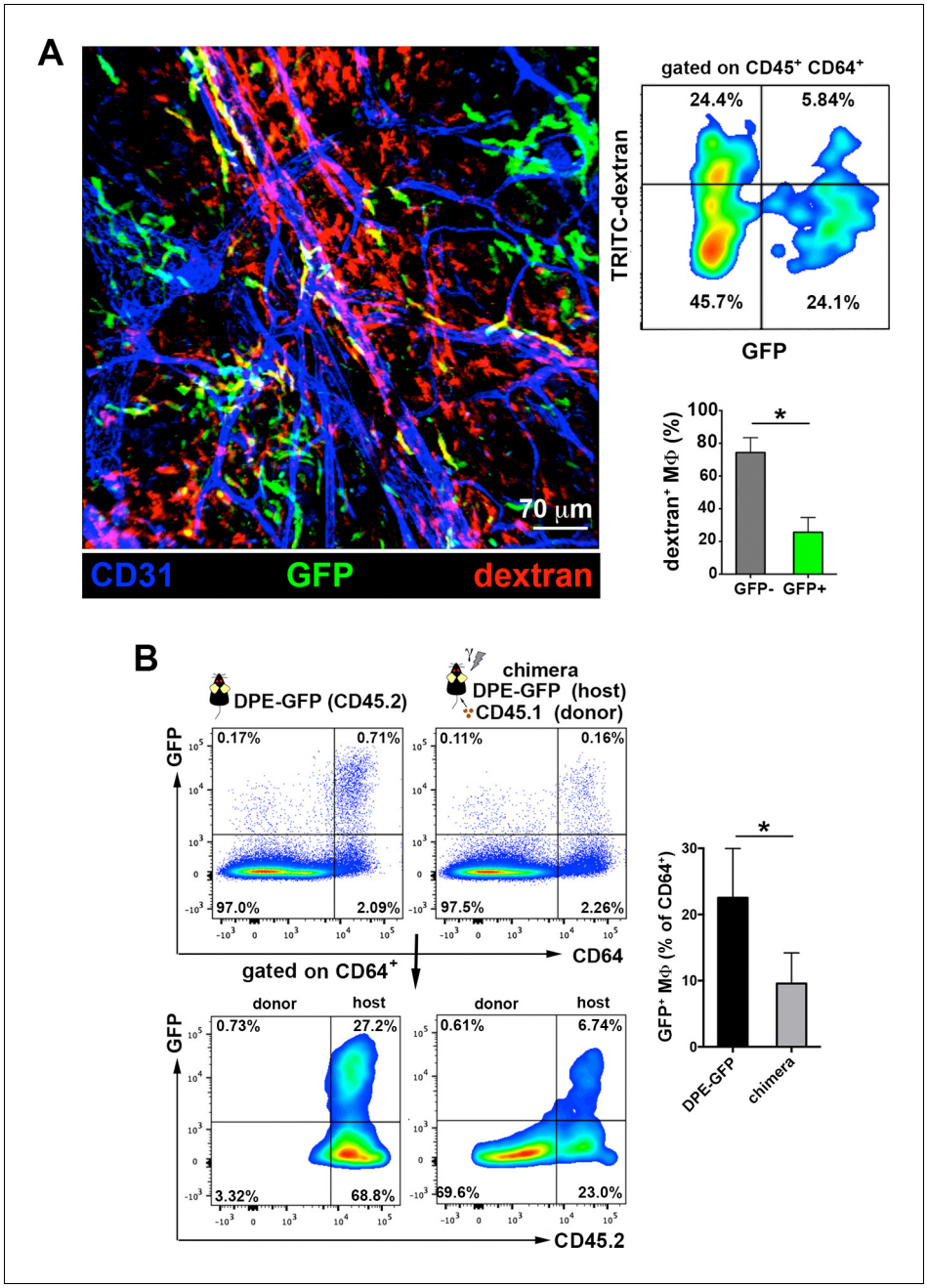

Figure 4. The perivascular endothelium-protruding macrophages are distinct from the perivascular DPE-GFP$^+$ macrophages. (**A**) (Left) Maximal projection of the ear dermis of a DPE-GFP animal injected i.v. with HMw TRITC-dextran, fixed and stained with anti-CD31. The 3D colocalization analysis of the green (GFP$^+$ perivascular MΦ) and red (dextran$^+$ perivascular MΦ) signals was estimated (Pearson's coefficient in colocalized volume = 0.1901). (Upper right) FACS analysis of macrophages in ear skin from DPE-GFP animals injected i.v. with HMw TRITC-dextran. (Lower right) Bar histogram showing contribution of GFP$^-$ and $^+$ subsets to the pool of dextran$^+$ macrophages. Values are mean ± SD (n = 3). Statistical significance was assessed by unpaired two-tailed Student's t-test (* $p<0.05$). (**B**) DPE-GFP CD45.2 animals were lethally irradiated and reconstituted with wt congenic CD45.1 BM. Animals were sacrificed 1 month later and the content of skin GFP$^+$ MΦ in their skin was analyzed by FACS and compared with untreated DPE-GFP CD45.2 animals. The bar histogram on the right shows the % of GFP$^+$ macrophages out of total skin macrophages. Data are mean ± SD (n = 4). Statistical significance was assessed by unpaired two-tailed Student's t-test (* $p<0.05$).

DOI: 10.7554/eLife.15251.016

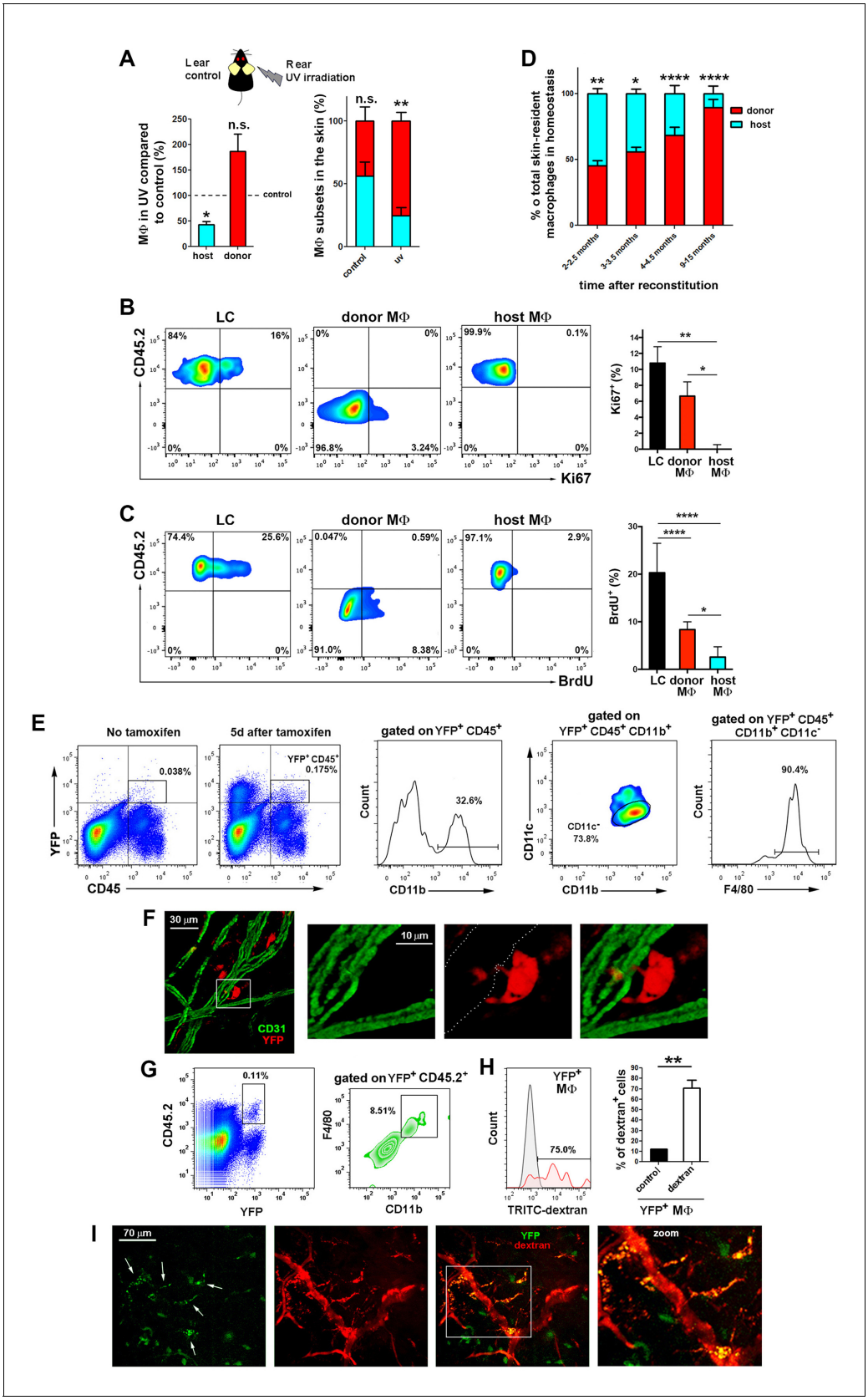

Figure 5. The skin radioresistant macrophages are an UV-sensitive population endowed with in situ renewal potential from an extramedullary progenitor. (**A**) Ears from chimeric animals (CD45.1(donor)/CD45.2(host)) were analyzed by flow cytometry 4 weeks after irradiation with UV-A/B or no

Figure 5 continued on next page

Figure 5 continued

irradiation. The left bar histogram shows the percentage of remaining macrophages of each haplotype after UV irradiation relative to untreated controls (n = 3/group). The second bar histogram depicts the relative content of each subset out of the total pool of tissue-resident macrophages in treated and non-treated animals. Data are means ± SEM. Statistical significance was assessed by two-way ANOVA analysis with Sidak's post-test (left) and one-sample t-test referred to value = 100 (right) (n.s. not significant, **p-value < 0.01). (**B**) Ki-67 staining reveals the lack of self-renewal capacity of radioresistant host macrophages in steady-state. Chimeric mice (CD45.1-donor/CD45.2-host) reconstituted for 3 months were sacrificed and skin processed and stained with anti-Ki-67 for FACS analysis. Tissue-resident macrophages from host ($CD45.2^+$ and $CD64^+$) and donor ($CD45.1^+$ and $CD64^+$) as well as Langerhans cells (LC, $CD45.2^+$ $CD326^+$ and $MHC\text{-}II^+$, used as control subset endowed with self-renewal capacity) were analyzed. Values are mean ± SEM (n = 4). Statistical significance was assessed by one-way ANOVA with Dunnett's post-test (*p-value < 0.05, **p-value < 0.005). (**C**) BrdU tracing revealed the slower turnover rate of host radioresistant macrophages. Chimeric mice (CD45.1-donor/CD45.2-host) were treated with BrdU in drinking water ad libitum. Animals were sacrificed 8 d later and skin processed for BrdU staining. Tissue-resident macrophages from host and donor as well as Langerhans cells were analyzed. Values are mean ± SD (n = 4). Statistical significance was assessed by one-way ANOVA with Tukey's post-test (**p-value < 0.005, ****p-value < 0.0001). (**D**) Fluctuations over time in the relative content of host and donor macrophages in the homeostatic skin of chimeric animals (n = 5/group). Data are mean ± SD. Statistical significance was assessed by two-way ANOVA with Sidak's post-test (*p-value < 0.05, **p-value < 0.01, ***p-value < 0.005, ****p-value < 0.0001). (**E**) Ears from tamoxifen-treated *Bmi1*-IRES-Cre-ERT2 Rosa26 YFP reporter mice were analyzed by flow cytometry 5d after treatment. Representative FACS analysis of the identified YFP^+CD45^+ fraction is shown. (**F**) Whole-mount staining of an ear from a tamoxifen-treated *Bmi1*-IRES-Cre-ERT2 Rosa26 YFP mouse. The boxed area highlights a YFP^+ perivascular cell protruding into a vessel, shown at high magnification in the accompanying panels. The white-dotted line marks the vasculature in the red channel. (**G**) *Bmi1*-IRES-Cre-ERT2 Rosa26 YFP CD45.2 host mice were chimerized with bone marrow from CD45.1 wt donors. Ears of these chimeric mice were analyzed by FACS and a subset of $YFP^+CD11b^+F4/80^{high}$ myeloid cells was detected. (**H**) FACS analysis of *Bmi1*-IRES-Cre-ERT2 Rosa26 YFP chimeric mice injected with HMw dextran. The bar histogram represents the percentage of YFP^+ $dextran^+$ macrophages respect to untreated control (n = 4). Data are mean ± SD. Statistical significance was assessed by unpaired two-tailed Student's t-test (**p-value < 0.01). (**I**) Representative intravital images of the ear of a chimeric mouse generated as in G, and injected with HMw TRITC-dextran. White arrows in the green channel mark $YFP^+dextran^+$ perivascular cells.
DOI: 10.7554/eLife.15251.017

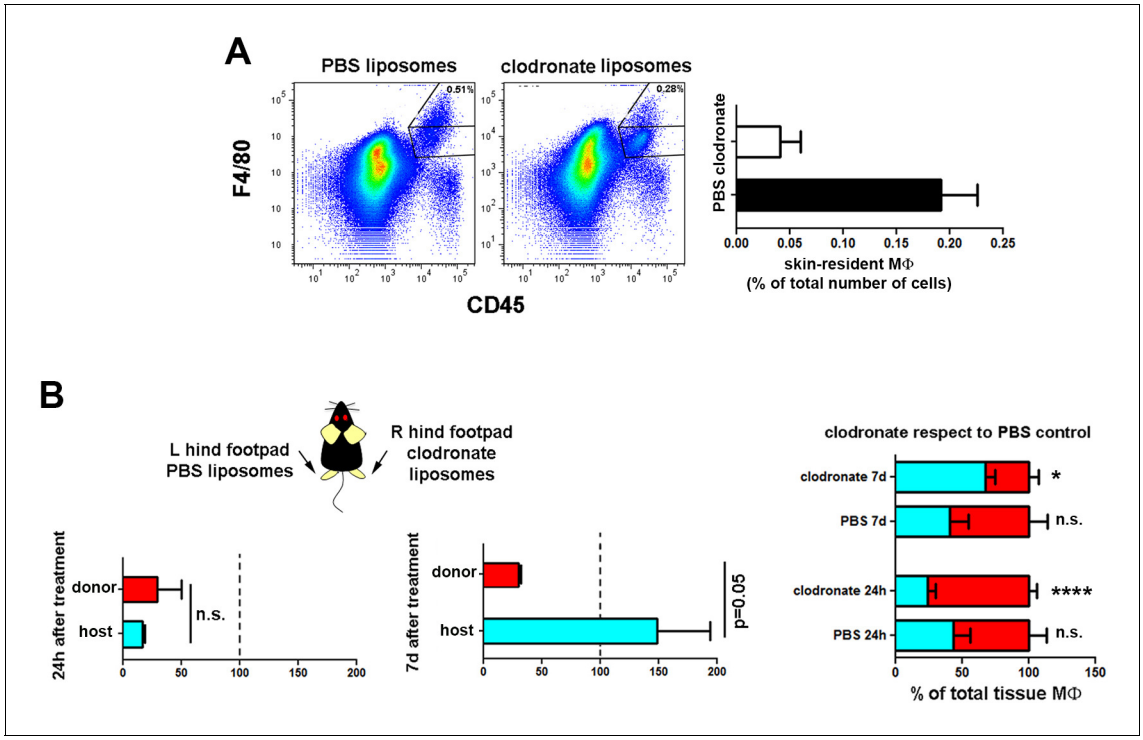

Figure 5—figure supplement 1. Selective recovery of host macrophages in chimeric animals treated with clodronate liposomes intradermally. (**A**) Mouse hind footpads were injected intradermally with clodronate or PBS liposomes, and animals were sacrificed 24 hr later. (Upper) Representative dot plots show the partial depletion of the skin macrophage pool after clodronate treatment. (Lower) Bar histogram comparing the percentage of tissue-resident macrophages in PBS- and clodronate-treated skins. (**B**) Mouse hind footpads were intradermally injected either with clodronate or PBS liposomes and animals were sacrificed 24 hr or 7d after treatment (Upper) The bar histograms show the percentage of macrophages of each haplotype remaining after the indicated post-clodronate times relative to untreated controls (n = 3/group). (Lower) The bar histogram shows the relative content of each type out of the total pool of tissue-resident macrophages in treated and non-treated ears. (n = 4). Statistical significance was assessed (upper) by unpaired two-tailed Student's t-test (n.s. not significant, p-value = 0.05) and (lower) by two-way ANOVA with Sidak's post-test (*p<0.05, ****p<0.0001).

DOI: 10.7554/eLife.15251.018

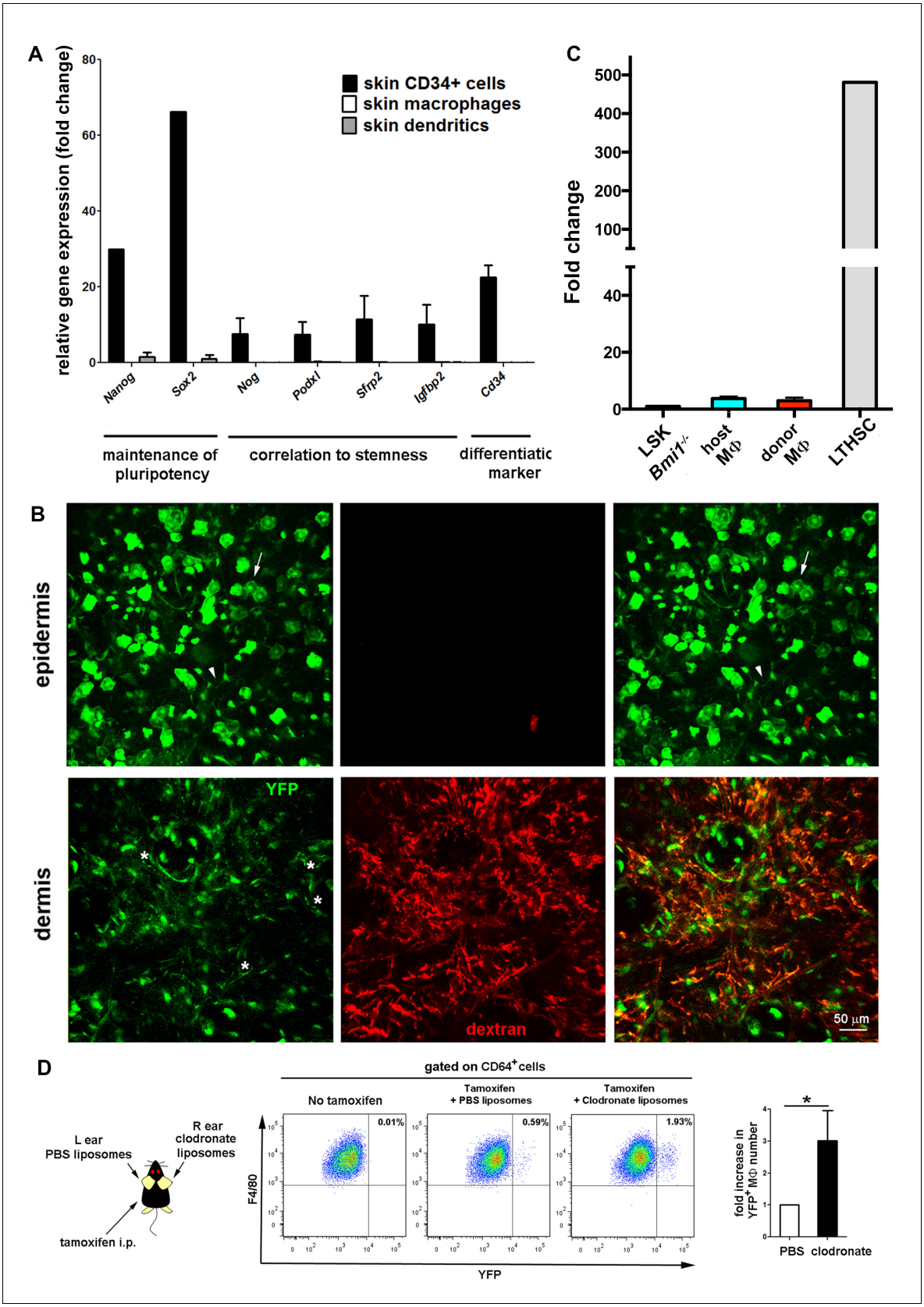

Figure 5—figure supplement 2. Absence of stemness gene expression in skin resident macrophages in steady-state. (**A**) qPCR analysis of the expression of stemness-related genes in skin macrophages, dendritic cells and a skin CD34^{+} cell pool. Data are means of normalized values obtained

Figure 5—figure supplement 2 continued on next page

Figure 5—figure supplement 2 continued

from two independent samples. Bars represent mean ± S.E.M. in all cases. (**B**) qPCR analysis of *Bmi1* gene expression in the different subsets of tissue-resident macrophages expressed as fold change using as housekeeping gene *Gapdh*. We used LSK cells from an inducible *Bmi1*$^{-/-}$ animal treated with tamoxifen as negative control and long-term hematopoietic stem cells from a wt animal as positive control. Data are means of normalized values obtained from two independent samples. Bars represent mean ± SD. (**C**) Assessment of driver induction in the skin of *Bmi1*-IRES-Cre-ERT2 Rosa26 YFP animals. Maximal projections of z-stacks of ear dermis and epidermis from a chimeric wt CD45.1/*Bmi1* cre-IRES ERT2 Rosa26YFP CD45.2 animal (donor/host) treated with tamoxifen and injected with HMw TRITC-dextran. The white arrow points to YFP^{+} cells with a morphology compatible with keratinocytes in the epidermis. The white arrowhead indicates an YFP^{+} cell with dendritic morphology that corresponds to a γδ epidermal T cell (FACS analysis not shown). The white asterisks (green channel) mark selected YFP^{+} dextran^{+} perivascular cells found in the dermis. (**D**) *Bmi1*-IRES-Cre-ERT2 Rosa26 YFP reporter mice were intradermally injected in the ears either with PBS or clodronate liposomes and simultaneously i.p. injected with tamoxifen. After 15d, ears were harvested and their content in YFP+ macrophages (defined as CD64+ F4/80+ cells) was analyzed by flow cytometry. Statistical significance was assessed by unpaired two-tailed Student's t-test (*p-value < 0.05).

DOI: 10.7554/eLife.15251.019

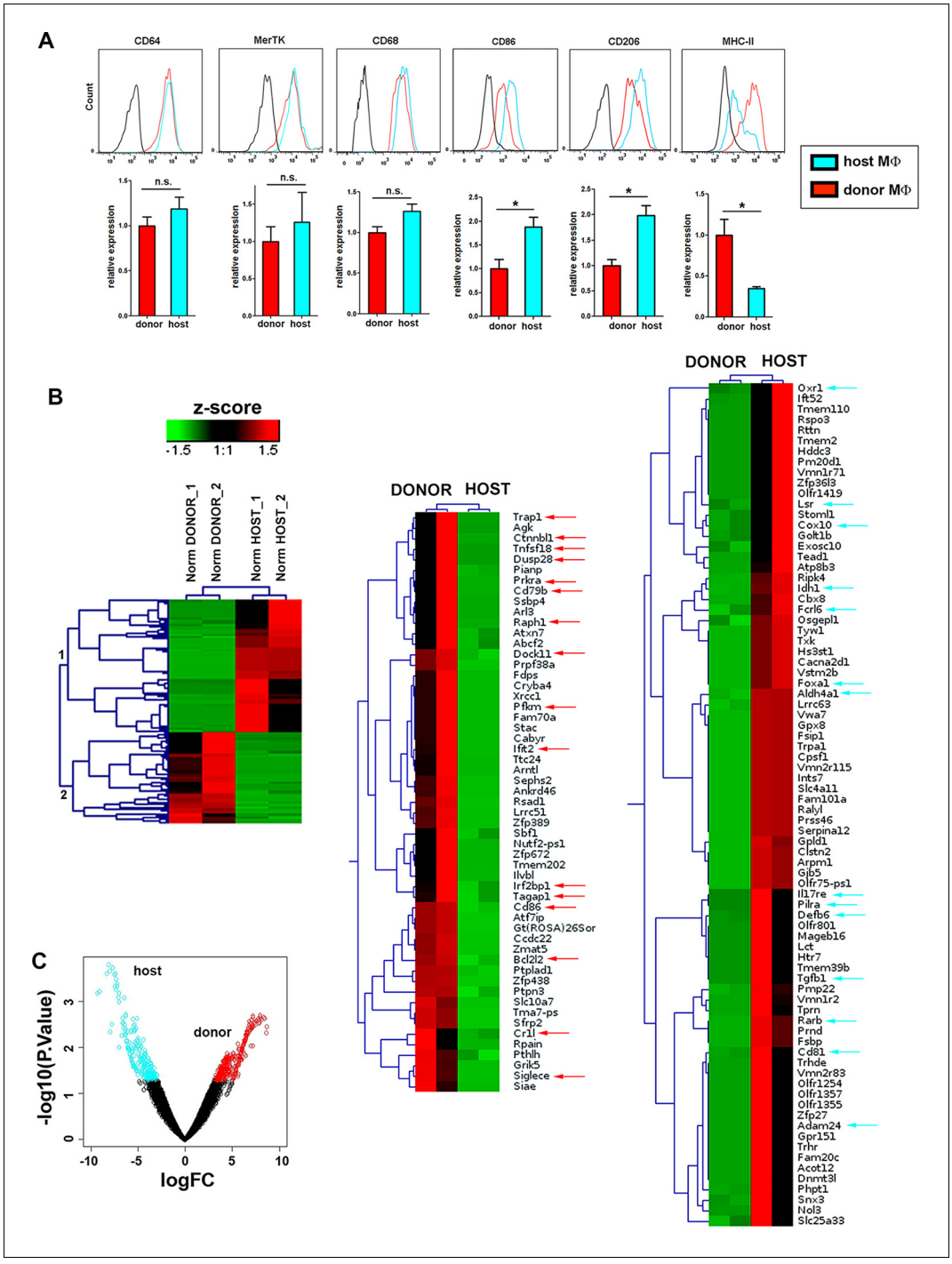

Figure 6. Phenotypic and RNASeq analyses of donor and host skin-resident macrophages from chimeric animals. (**A**) Flow cytometry analysis of the surface expression of macrophage-specific markers (CD64, MerTK, CD68), as well as CD86, CD206 and MHC-II in donor and host macrophages from chimeric animals in steady-state. Values correspond to the normalized average GeoMean ± SD (n = 3). Statistical significance was assessed by unpaired two-tailed Student's t-test (n.s. not significant, *p-value < 0.05, **p-value < 0.01). (**B**) (Left) Compact view of the hierarchical clustering of the normalized expression profiles of the protein coding sequences with p-value <= 0.05 and consistent expression levels across replicates. (Center and right) Detailed view of the hierarchical clustering showing gene annotation. Arrows highlight relevant genes upregulated in host (blue) and donor (red). (**C**) Vulcano plot representing the log2FC vs –log10 p-value transformation. Highlighted points correspond to genes with a p-

Figure 6 continued on next page

Figure 6 continued

value smaller than 0.05 (blue for genes more expressed in host than donor and red for genes with the opposite expression profile).

DOI: 10.7554/eLife.15251.020

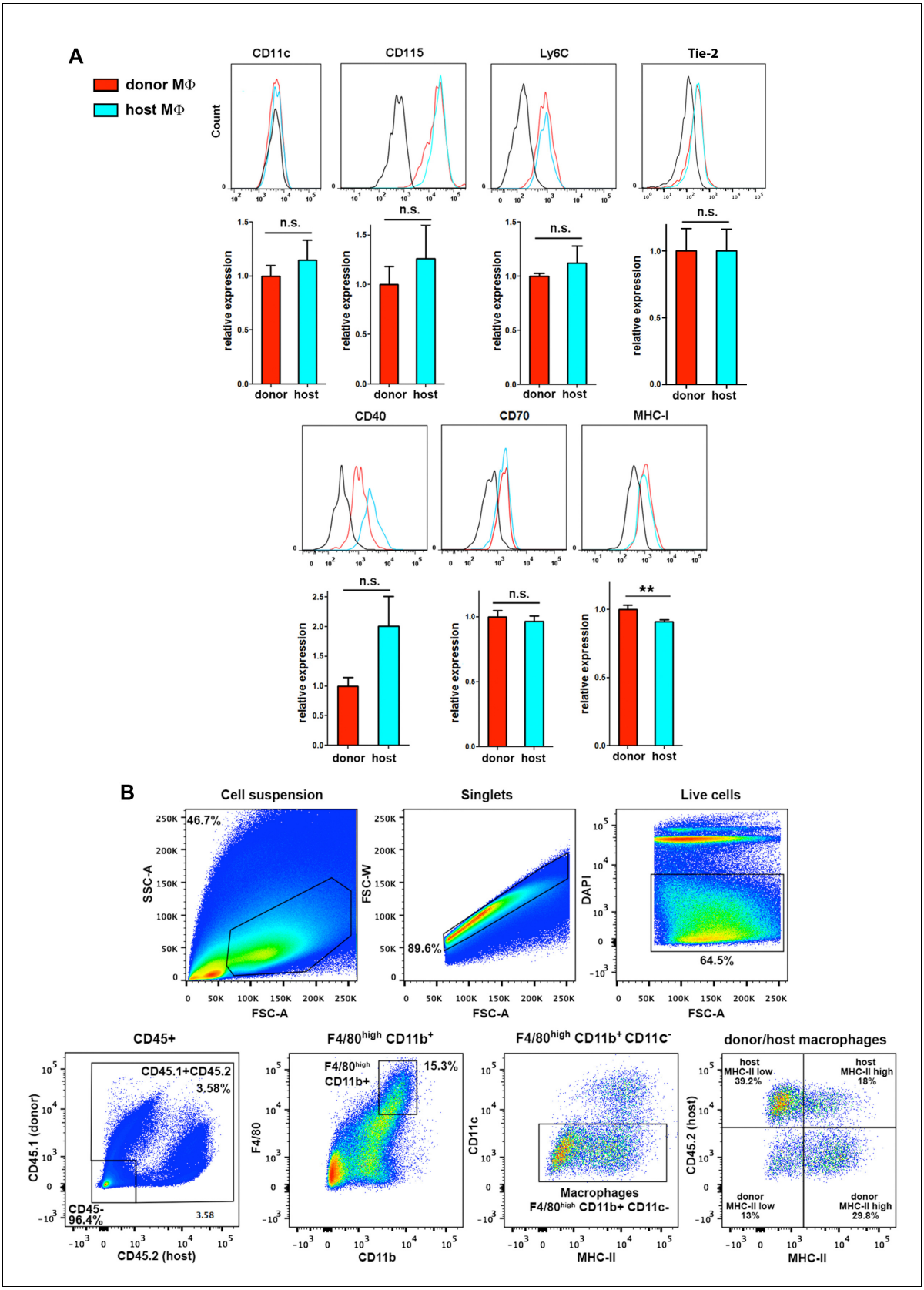

Figure 6—figure supplement 1. Extended phenotypic analysis of host and donor skin-resident macrophages. (**A**) Flow cytometry analysis of the surface expression of myeloid-specific markers (CD11c, CD115, Ly6C), as well as Tie-2, CD40, CD70 and MHC-I in donor and host macrophages from

Figure 6—figure supplement 1 continued on next page

Figure 6—figure supplement 1 continued

chimeric animals in steady-state. Values correspond to the normalized average GeoMean ± SD (n = 3). Statistical significance was assessed by unpaired two-tailed Student's t-test (n.s. not significant, **p-value < 0.01). (**B**) MHC-II expression does not accurately discriminate radio-resistant host from BM-derived donor macrophages. Single-cell suspensions obtained by enzymatic digestion and gentle dissociation of the ear skin were gated to exclude doublets and dead cells (DAPI staining). Then, macrophages were gated as $CD45^{+}$, $F4/80^{high}$, $CD11b^{+}$, $CD11c^{-}$ and the expression of MHC-II was separately analyzed in the host ($CD45.2^{+}$) and donor ($CD45.1^{+}$) subsets. MHC-II^{low} macrophages correspond to the P4 subset and MHC-II^{high} macrophages to the P5 subset in the classification reported by Tamoutounour and colleagues. Representative dot plots are shown.

DOI: 10.7554/eLife.15251.021

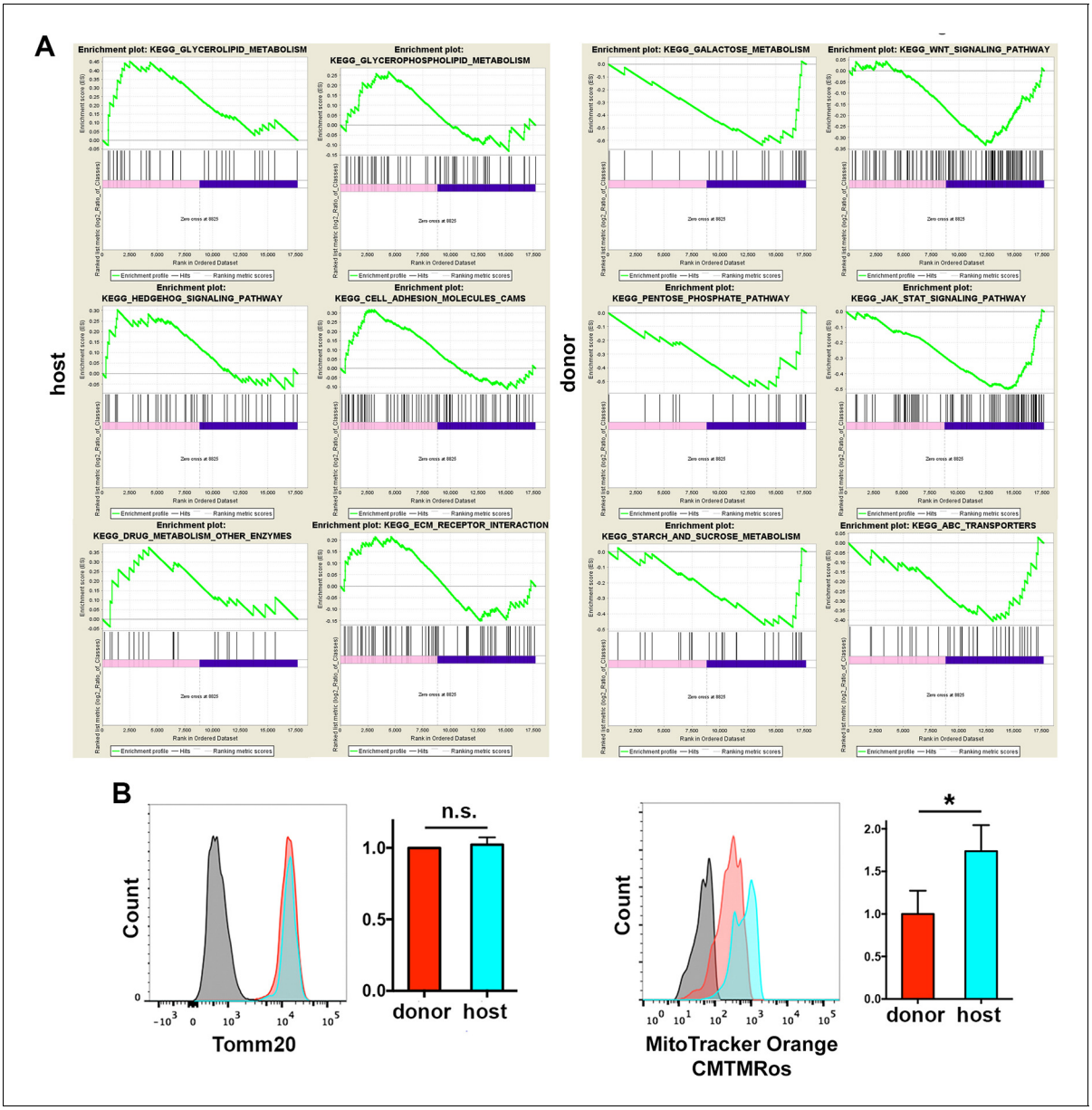

Figure 6—figure supplement 2. GSEA of the RNASeq data. Mitochondrial function in skin macrophages. (**A**) Selected enrichment plots of Kegg pathways selectively increased in host or donor macrophages from the GSEA in ***Supplementary file 2*** are shown. (**B**) Representative FACS histograms show the mitochondrial content and function in skin-resident macrophage subsets of chimeric mice. Briefly, ears were collected and both halves separated and incubated with MitoTracker Orange CMTMRos. Then, tissue was processed and single-cell suspensions analyzed by flow cytometry for mitochondrial content–Tomm20 staining- (left) and mitochondrial membrane potential (function) –mitotracker- (right). Values are normalized average GeoMean ± SD (n = 3). Statistical significance was assessed by unpaired two-tailed Student's t-test (n.s. not significant, *p<0.05).

DOI: 10.7554/eLife.15251.022

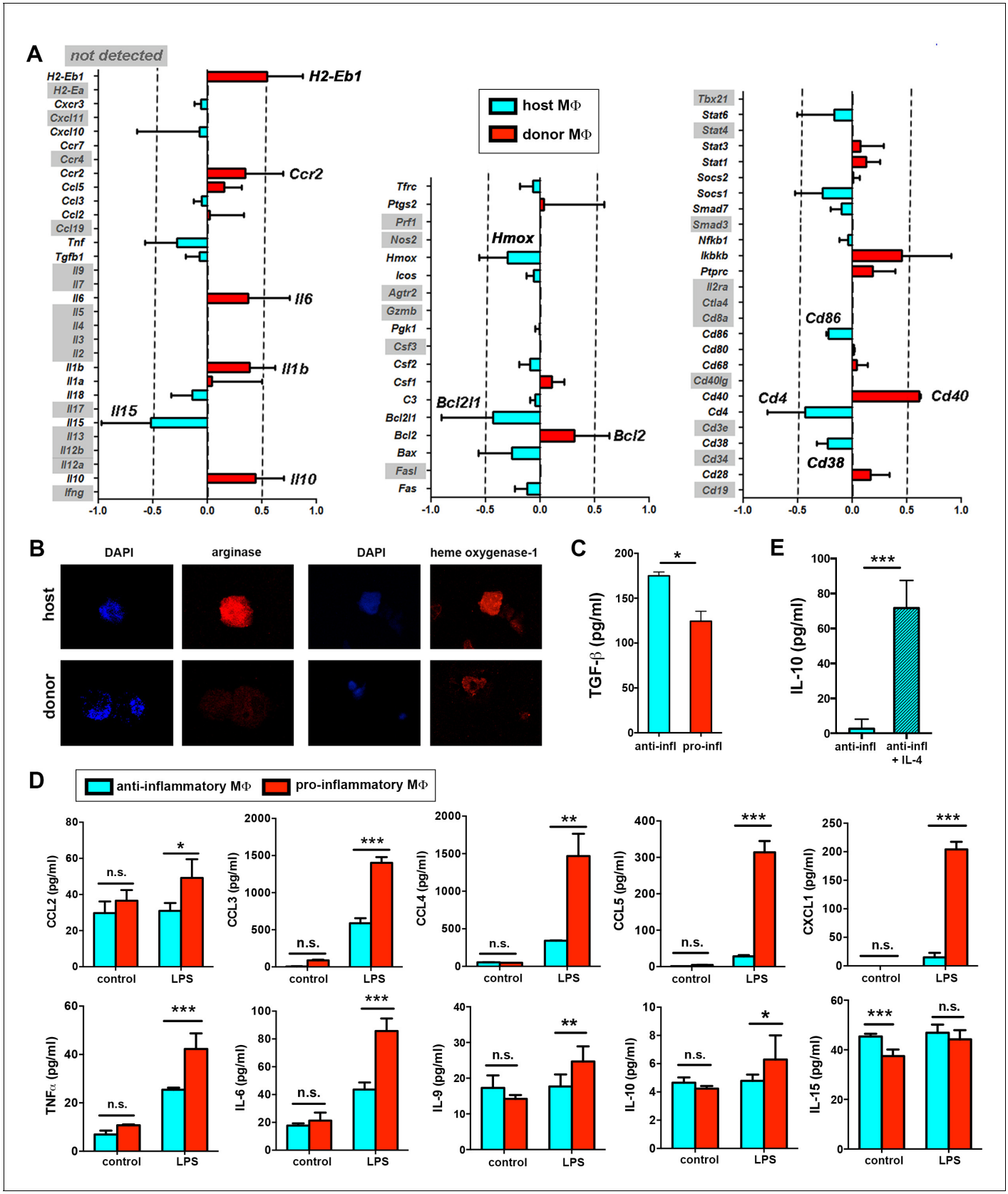

Figure 7. Immune transcriptional profile and polarization potential of STREAMs. (**A**) Comparative qPCR analysis of immune response-related genes in donor and host skin macrophages from chimeric mice. Data represent average logFC values ± SEM (n = 4). (**B**) Immunostaining of anti-inflammatory

Figure 7 continued on next page

Figure 7 continued

markers arginase I and heme oxygenase-1 in cytospin samples of isolated macrophage subsets (donor and host from chimeric animals). (**C**) ELISA quantification of TGF-β secretion by anti-inflammatory and pro-inflammatory macrophages at steady-state. Data are mean value ± SD (n = 4). Statistical significance was assessed by unpaired two-tailed Student's t-test (*p<0.05). (**D**) Sorted pro-inflammatory and anti-inflammatory MΦ were left untreated or treated with 1 ng/ml LPS for 24 hr. Then, a multiplex flow cytometry-based analysis of culture supernatants was performed. Data are mean ± SD (n = 3–5). Statistical significance was assessed by two-way ANOVA with Bonferroni's post-test (n.s. not significant, *p-value < 0.05, ** p-value < 0.01, ***p-value < 0.005). (**E**) ELISA quantification of IL-10 secretion by anti-inflammatory macrophages (50.000 cells/100 µl RPMI medium) at steady-state and after IL-4 stimulation (20 ng/ml) for 24 hr. Data are mean value ± SD (n = 4). Statistical significance was assessed by unpaired two-tailed Student's t-test (***p-value < 0.005).

DOI: 10.7554/eLife.15251.023

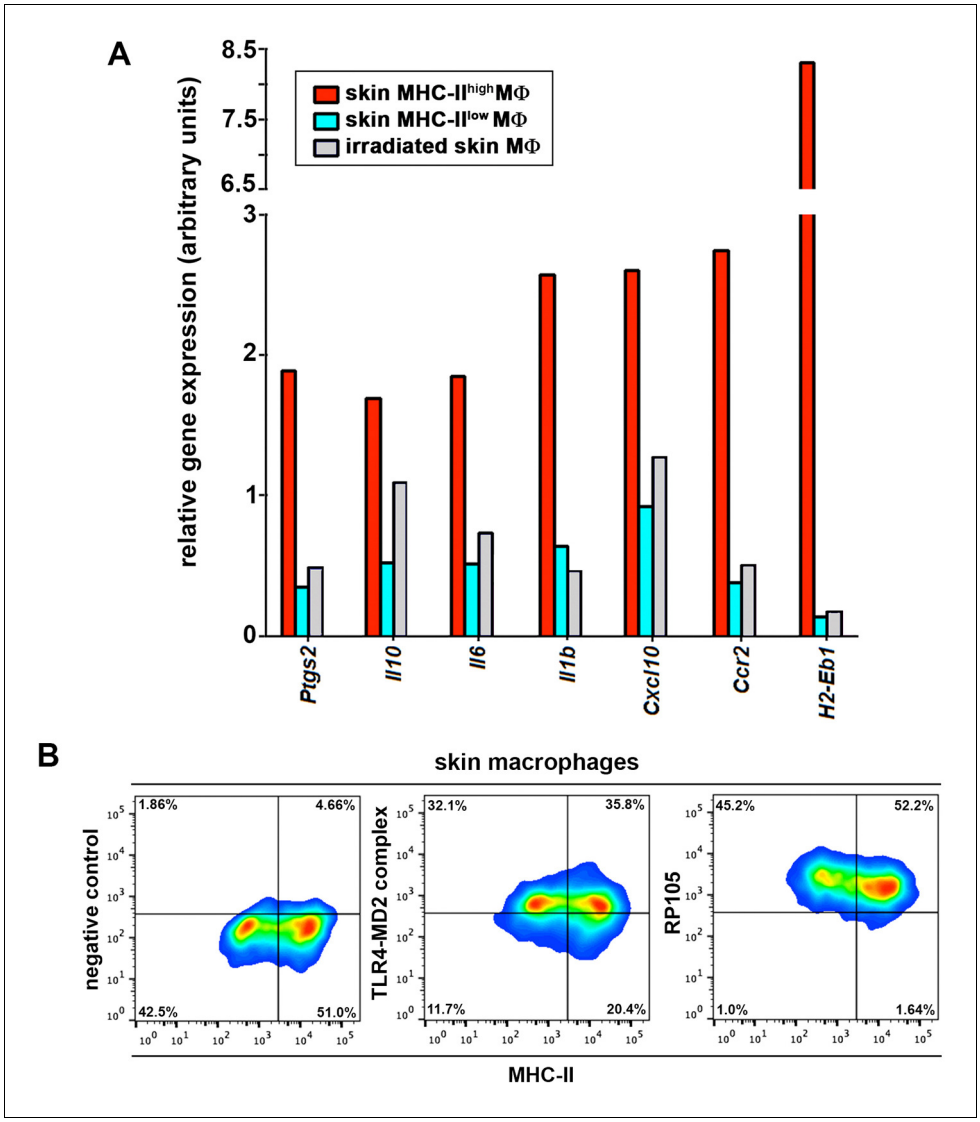

Figure 7—figure supplement 1. Gene profile of skin macrophages from non-treated and γ-irradiated animals. LPS receptor expression in skin macrophages. (**A**) Representative qPCR analysis of pro-inflammatory genes in samples from skin-resident MHC^{low} and MHCII^{high} macrophage subsets in steady state or remaining skin-resident macrophages 7d after γ-irradiation. (**B**) Representative FACS dot plots showing the expression of the LPS receptors TLR4-MD2 complex and RP105 in skin macrophages from control C57BL/6 mice.
DOI: 10.7554/eLife.15251.024

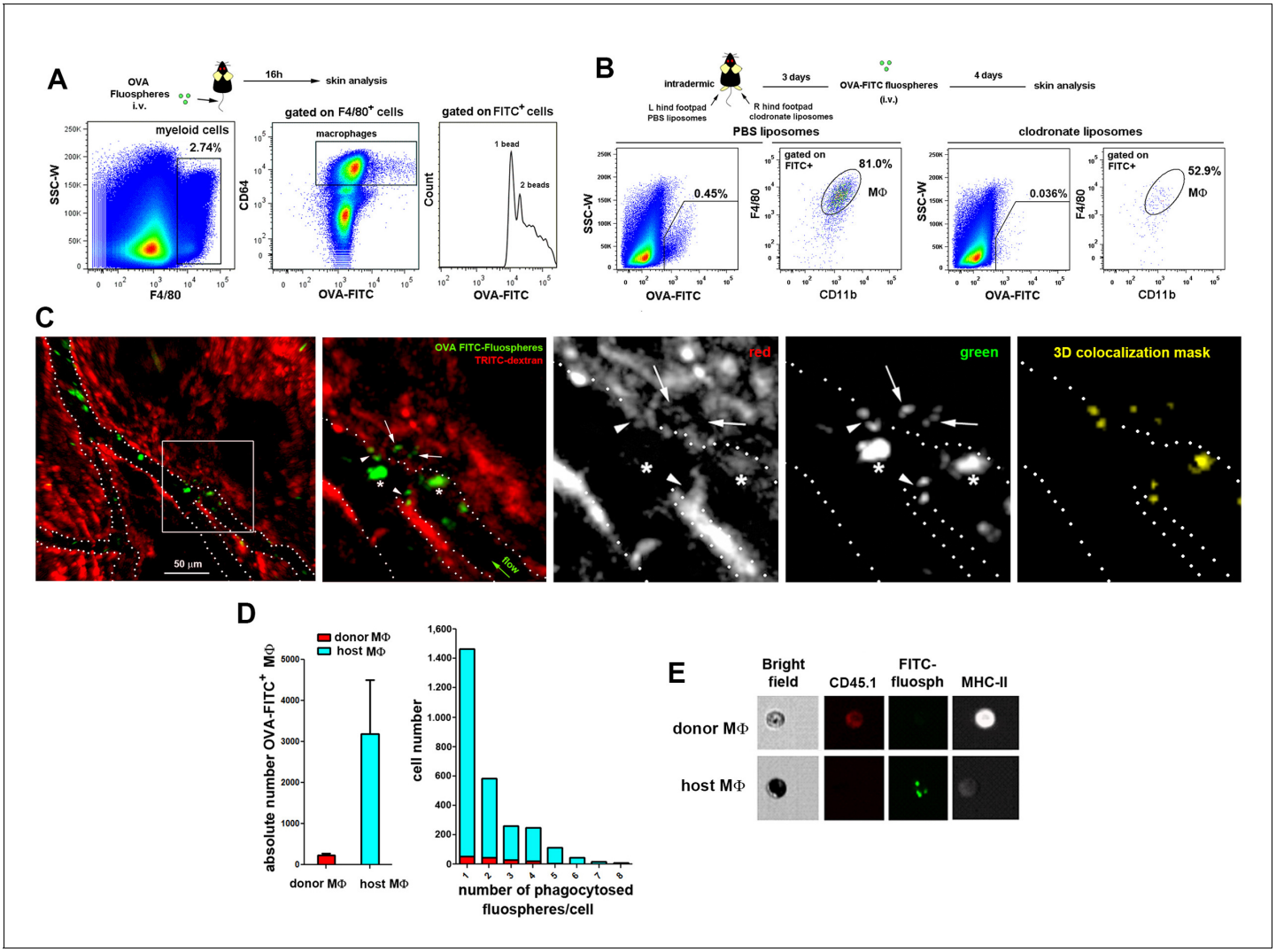

Figure 8. STREAMs capture blood-borne OVA nanoparticles at steady-state. (**A**) Representative flow cytometry analysis of OVA-FITC fluosphere capture by skin macrophages in C57BL/6 mice. The peaks observed in the histogram correspond to the number of fluospheres uptake per cell. (**B**) Mice were intradermally injected with PBS (control) or clodronate liposomes in the hind footpads and were injected i.v. with OVA-adsorbed FITC fluospheres 72 hr later, followed by analysis after 4d. Representative dot plots show the amount of FITC$^+$ cells for each treatment and histograms show the proportion of MΦ in the FITC$^+$ fraction. (**C**) (Left) A C57BL/6 mouse was first injected i.v. with HMw TRITC-dextran and with OVA-FITC fluospheres 16 hr later. Imaging began 24 hr after the last injection. A representative frame of the experiment extracted from ***Video 8*** with zoomed detail aside is shown. White dotted lines depict vessel walls. White asterisks mark FITC$^+$ intravascular monocytes that have phagocytosed OVA fluospheres. White arrowheads point to intraluminal particles retained by dextran$^+$ STREAMs and white arrows point to extravascular particles already phagocytosed by STREAMs. (Center and right) Split channels are shown with higher magnification as well as a 3D colocalization mask of both channels. (**D**) (Left) Absolute number of macrophages of each haplotype (CD45.1 (donor) or CD45.2 (host)) that have captured OVA-coated fluospheres in treated chimeric animals (n = 4). Data are means ± SEM. (Right) Representative per-cell uptake of fluospheres by macrophages of each haplotype. (**E**) Single-cell images of sorted skin macrophage subsets of a chimeric mouse (CD45.1/CD45.2, donor/host) injected i.v. with OVA-FITC fluospheres. Images were obtained using an imaging flow cytometer. Notably, host macrophages were mostly filled with melanin as confirmed with Fontana-Masson staining (*data not shown*).

DOI: 10.7554/eLife.15251.025

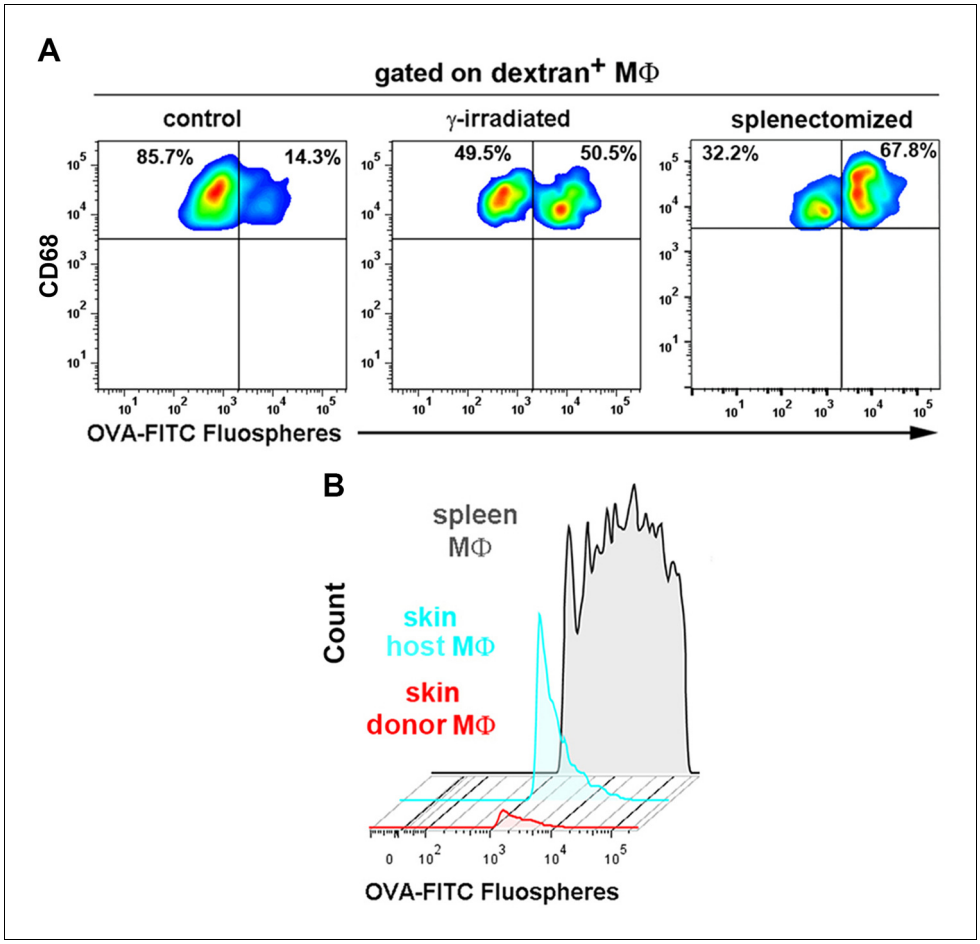

Figure 8—figure supplement 1. Comparison of OVA-FITC fluosphere uptake either by skin dextran$^+$ macrophages in control, γ-irradiated and splenectomized animals or by spleen macrophages and skin macrophage subsets in chimeric mice. (**A**) Control, γ-irradiated and splenectomized mice were injected i.v. with HMw TRICT-dextran and, 16 hr later, with OVA-coated FITC-fluospheres. Then, animals were sacrificed 3d later and dextran$^+$ cells were analyzed for their content in fluospheres. Representative FACS dot plots are shown. (**B**) Chimeric CD45.1 (donor)/CD45.2 (host) animals were injected i.v. with OVA-FITC fluospheres and sacrificed 3d later. FITC$^+$ macrophage subsets from spleen and ear were plotted on the same histogram. The splenic macrophages displayed a wide range of phagocytic capacity (from 1 fluosphere up to more than 10 per cell), whereas skin host macrophages could mostly phagocytose 1–2 fluospheres per cell. Skin donor macrophages were unable to phagocytose intravascular fluospheres.

DOI: 10.7554/eLife.15251.026

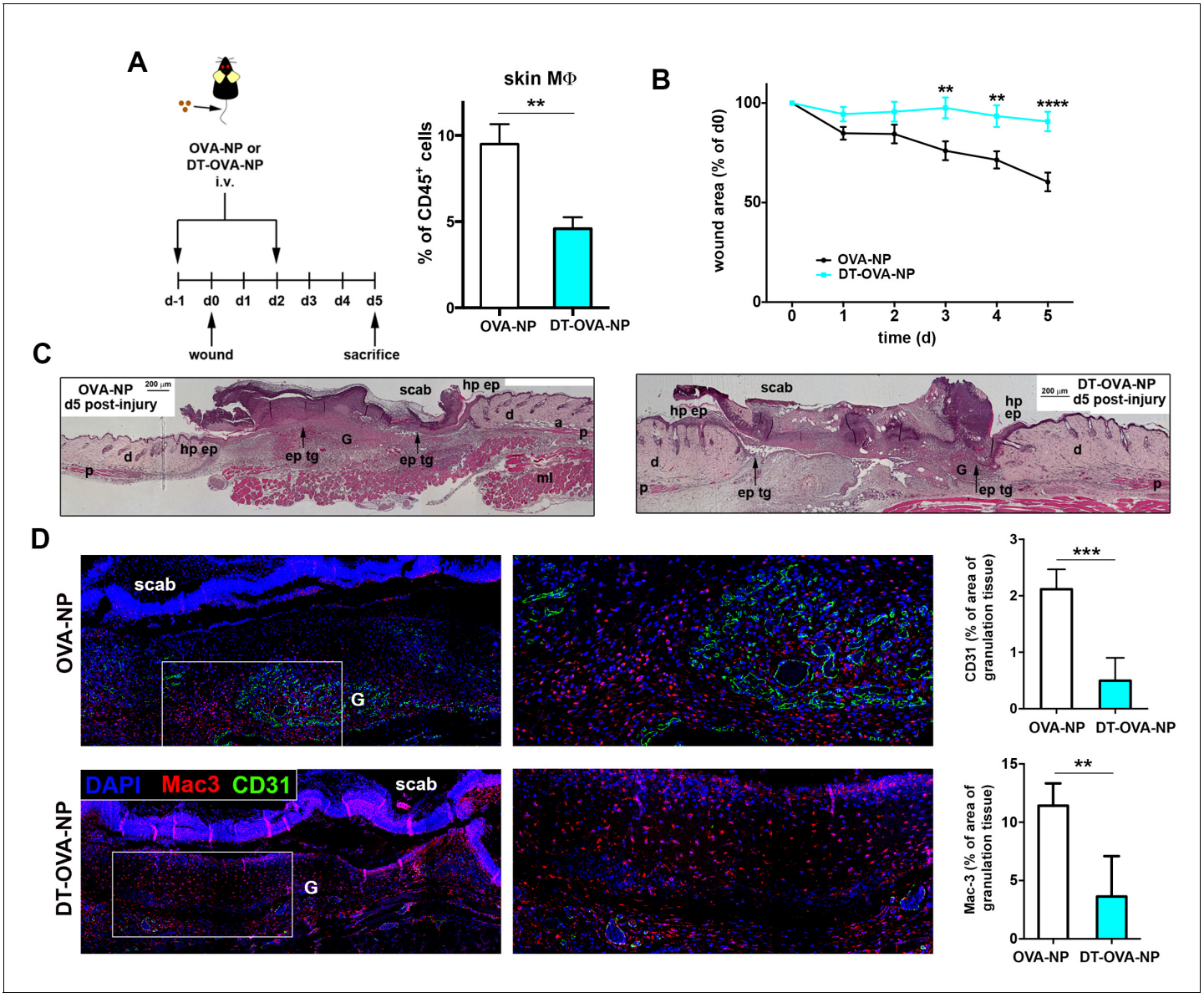

Figure 9. Macrophage depletion using DT-OVA-NP hampered wound healing. (**A**) (Left) Animals were first injected i.v. with either OVA-NP or DT-OVA-NP (2.5 µl/g) and, 1d later, the wound healing assay began. Two days after wounding, animals were treated with another similar dose of OVA-NP (control) or DT-OVA-NP. Then, mice were sacrificed 3d later (mid-stage repair) and their ears were collected to analyze skin macrophages. (Right) Bar histogram showing the percentage of MΦs out of total $CD45^+$ cells in the ears of OVA-NP- or DT-OVA-NP-treated animals. Data are mean ± SEM (n = 4–7). Statistical significance was assessed by unpaired two-tailed Student's t-test (**p-value < 0.01). (**B**) Analysis of mid-stage repair (5d after wounding). The plot illustrates the decrease of the wound area over time expressed as percentage of the initial wound. Data are mean SEM, n = 32 wounds/group. Statistical significance was assessed by two-way ANOVA analysis with Sidak's post-test (**p-value < 0.01, ****p-value < 0.0001) (**C**) Histological analysis of wounds at mid-stage of repair from OVA-NP- and DT-OVA-NP-treated animals. Hematoxylin-eosin staining of representative samples is shown. (Hp ep: hyperproliferative epithelium, ep tg: epithelial tongue, G: granulation tissue, d: dermis, p: panniculus carnosus, a: adipose tissue, ml: muscle layer). (**D**) (Left) Representative immunofluorescence staining of vessels (CD31 staining) and macrophages (Mac-3 staining) in tissue sections of wounds at mid-stage (5d) from OVA-NP- or DT-OVA-NP-treated animals. (Right) Quantification of CD31 and Mac-3 stained area within the granulation tissue is shown. Data are mean ± SD (n = 4–6). Statistical significance was assessed by unpaired two-tailed Student's t-test (**p<0.01, ***p<0.005).

DOI: 10.7554/eLife.15251.029

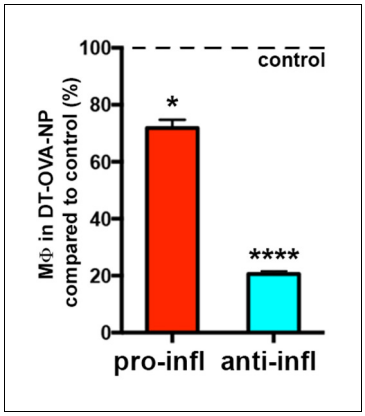

Figure 9—figure supplement 1. Selective deletion of STREAMs after DT-OVA-NP treatment. Bar histogram showing the fluctuations of anti- and pro-inflammatory MΦ subsets 48 hr after DT-OVA-NP treatment compared to control. Data are means ± SD (n = 3). Statistical significance was assessed one-sample t-test referred to value = 100 (*p-value < 0.05, ****p-value < 0.0001).

DOI: 10.7554/eLife.15251.030

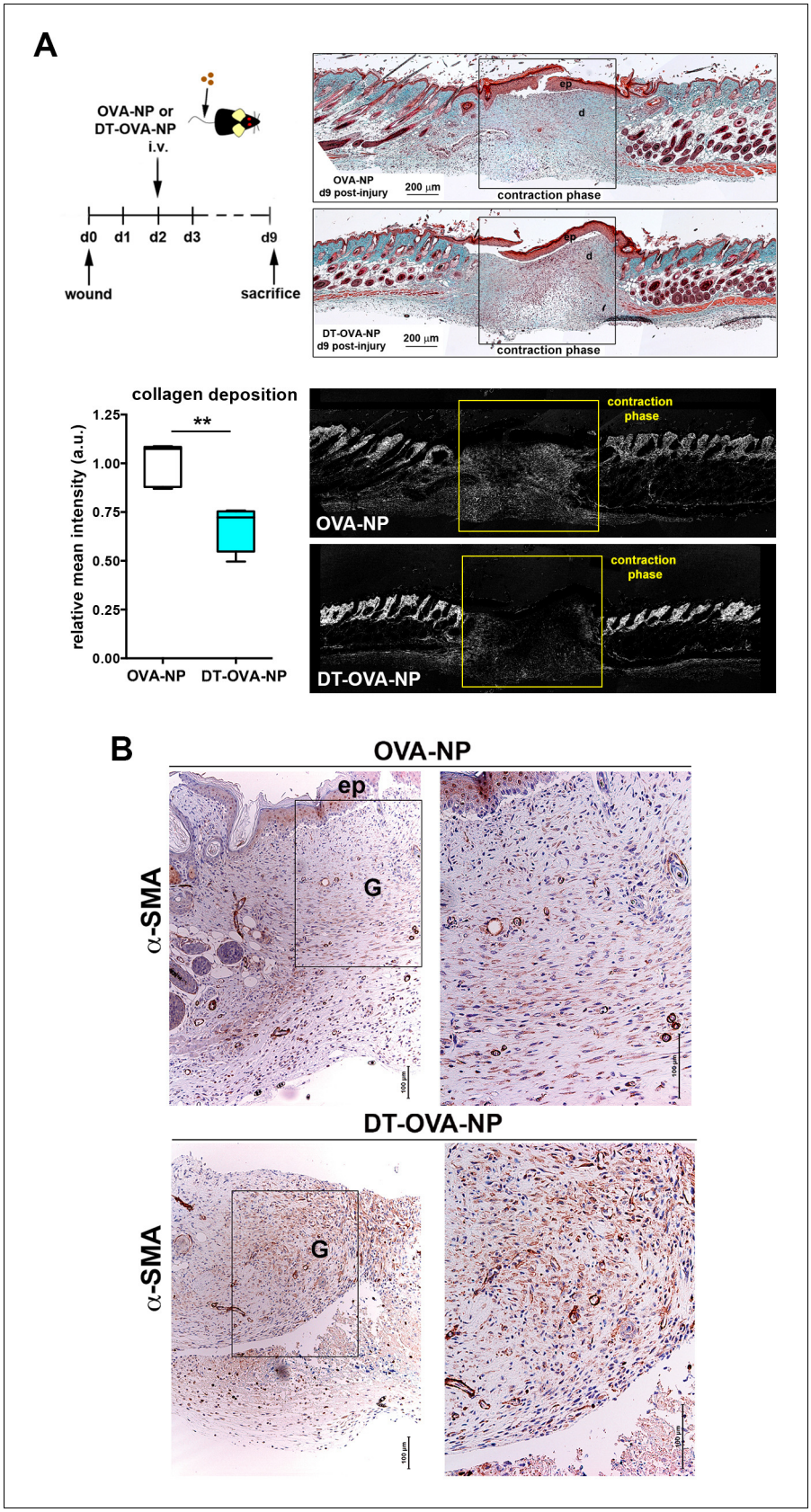

Figure 10. Macrophage depletion using DT-OVA-NP impaired collagen deposition and myofibroblast

Figure 10 continued on next page

Figure 10 continued

organization within the wound. (**A**) Wound healing assay until closure with administration of DT-OVA-NP or OVA-NP 2d after injury. After sacrifice, tissue was stained with hematoxylin-eosin (upper right) or analyzed for its content in collagen using Masson trichrome staining (lower right) followed by relative intensity quantification (n = 6/group) (lower left). Statistical significance was assessed by an unpaired two-tailed Student's t-test (**p<0.01). (Ep: epidermis, d: dermis). (**B**) Analysis of the myofibroblast distribution in the wound area at the time of closure (contraction phase) in OVA-NP and DT-OVA-NP mice. Immunohistochemical staining of α-SMA was performed. (Left) View of the complete wound, (right) zoom in the granulation tissue.

DOI: 10.7554/eLife.15251.031

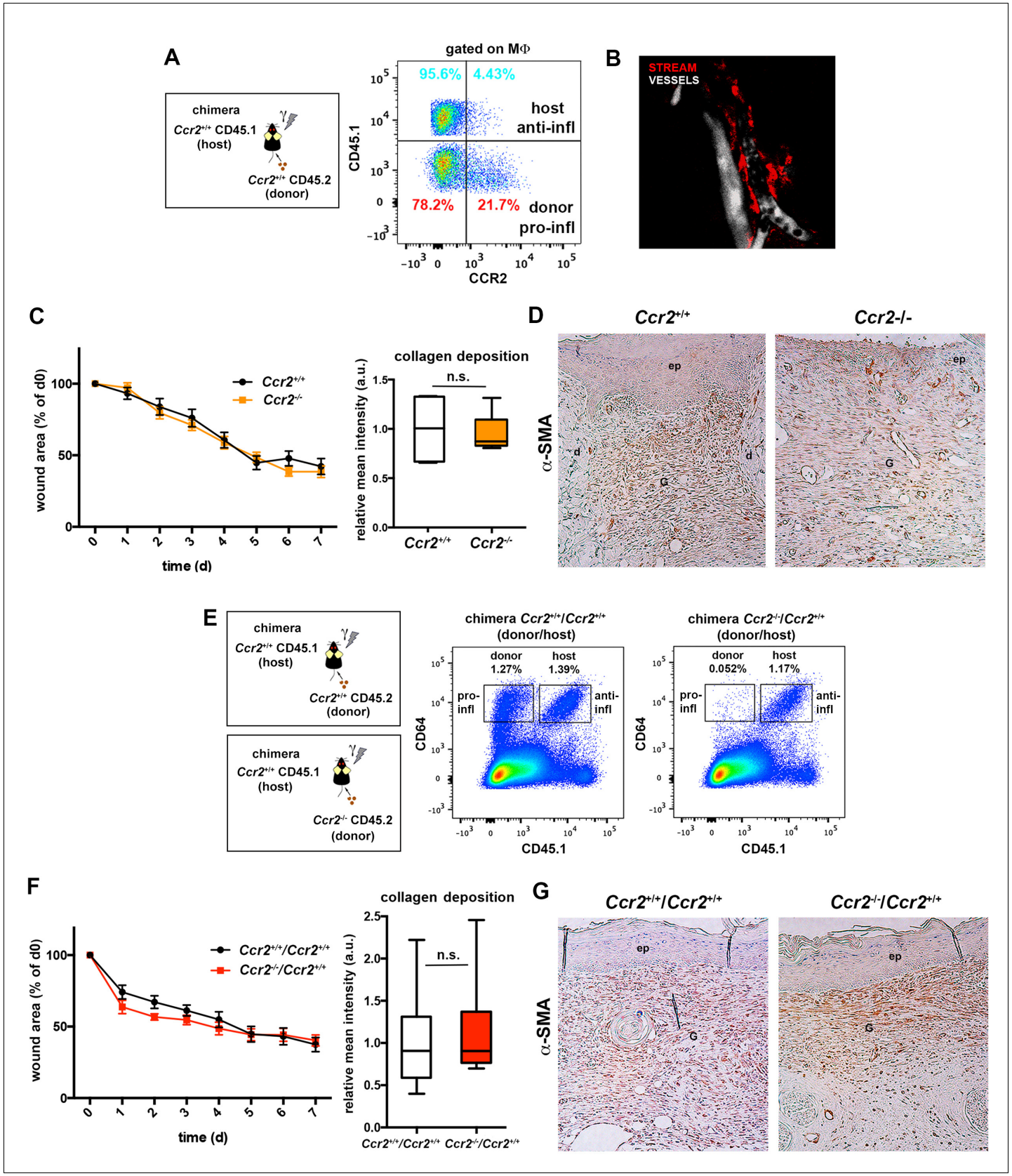

Figure 10—figure supplement 1. Skin-resident macrophages different from STREAMs are not critically involved in tissue repair. (**A**) Analysis of CCR2 expression in skin host and donor macrophages from CD45.1 (host)/CD45.2 (donor) chimeric animals. Representative FACS dot plot is shown. (**B**) A

Figure 10—figure supplement 1 continued on next page

Figure 10—figure supplement 1 continued

Ccr2$^{-/-}$ mouse was injected i.v. with HMw dextran and, 16 hr later, with a vascular tracer (vivotag). Intravital imaging revealed the presence of dextran^{+} STREAMs (red) around the vasculature (white). A maximal projection of a z-stack obtained from the ear dermis is depicted. (**C**) Wound healing assay until wound closure performed in *Ccr2*$^{+/+}$ and *Ccr2*$^{-/-}$ animals. (Left) The plots illustrate the decrease of the wound area over time expressed as percentage of the initial wound. Data are mean SEM, n = 28 wounds/group. Statistical significance was assessed by two-way ANOVA analysis with Sidak's post-test (differences were not found significant). (Right) Relative quantification of collagen deposition at the contraction phase (n = 6). Statistical significance was assessed by an unpaired two-tailed Student's t-test (n.s. not significant). (**D**) Immunohistochemical staining of α-SMA showing the distribution of myofibroblasts in the wound area at the time of closure in representative tissue sections of the two groups of animals. (**E**) Representative FACS dot plots showing the content of skin donor and host macrophages in the chimeric *Ccr2*$^{+/+}$(donor)/ *Ccr2*$^{+/+}$(host) and *Ccr2*$^{-/-}$(donor)/ *Ccr2*$^{+/+}$(host) mice. (**F**) Wound healing assay until wound closure performed in chimeric *Ccr2*$^{+/+}$/ *Ccr2*$^{+/+}$ vs. *Ccr2*$^{-/-}$/ *Ccr2*$^{+/+}$ (donor/host) animals. (Left) The plots illustrate the decrease of the wound area over time expressed as percentage of the initial wound. Data are mean ± SEM, n = 28 wounds/group. Statistical significance was assessed by two-way ANOVA analysis with Sidak's post-test (differences were not found significant). (Right) Relative quantification of collagen deposition at the contraction phase (n = 12/group). Statistical significance was assessed by an unpaired two-tailed Student's t-test (n.s. not significant). (**G**) Immunohistochemical staining of α-SMA showing the distribution of myofibroblasts in the wound area at the time of closure in representative tissue sections of the different chimeric animals.

DOI: 10.7554/eLife.15251.032